scientific reports

Check for updates

OPEN

Layer dependent thermal transport properties of one- to three-layer magnetic Fe:MoS_2

Elham Easy[1], Mengqi Fang[1], Mingxing Li[2], Eui-Hyeok Yang[1] & Xian Zhang[1]✉

Two-Dimensional transition metal dichalcogenides have been the subject of extensive attention thanks to their unique properties and atomically thin structure. Because of its unprecedented room-temperature magnetic properties, iron-doped MoS_2 (Fe:MoS_2) is considered the next-generation quantum and magnetic material. It is essential to understand Fe:MoS_2's thermal behavior since temperature and thermal load/activation are crucial for their magnetic properties and the current nano and quantum devices have been severely limited by thermal management. In this work, Fe:MoS_2 is synthesized by doping Fe atoms into MoS_2 using the chemical vapor deposition synthesis and a refined version of opto-thermal Raman technique is used to study the thermal transport properties of Fe:MoS_2 in the forms of single (1L), bilayer (2L), and tri-layer (3L). In the Opto-thermal Raman technique, a laser is focused on the center of a thin film and used to measure the peak position of a Raman-active mode. The lateral thermal conductivity of 1-3L of Fe:MoS_2 and the interfacial thermal conductance between Fe:MoS_2 and the substrate were obtained by analyzing the temperature-dependent and power-dependent Raman measurement, laser power absorption coefficient, and laser spot sizes. At the room temperature, the lateral thermal conductivity of 1-3L Fe:MoS_2 were discovered as 24 ± 11, 18 ± 9, and 16 ± 8 W/m·K, respectively which presents a decreasing trend from 1 to 3L and is about 40% lower than that of MoS_2. The interfacial thermal conductance of between Fe:MoS_2 and the substrate were discovered to be 0.3 ± 0.2, 1.1 ± 0.7, and 3.0 ± 2.3 MW/m^2·K for 1L to 3L respectively. We also characterized Fe:MoS_2's thermal transport at high temperature, and calculated Fe:MoS_2's thermal transport by density theory function. These findings will shed light on the thermal management and thermoelectric designs for Fe:MoS_2 based nano and quantum electronic devices.

Two-dimensional (2D) materials and their unique properties have attracted significant attention in recent years. With the discovery of graphene[1], transition metal dichalcogenides (TMDCs)[2,3] have been researched extensively due to their interesting thermal[4–8], electrical[9], thermoelectric[10], and optical[11,12] properties. Among them, MoS_2 is a layered semiconductor composed of covalently bonded transition-metal atoms (Mo) and chalcogen atoms (S)[13] with important applications in optoelectronic[14] and nano-electronic devices[15]. The thermal transport properties of 2D MoS_2 are very different from the bulk. Due to higher efficiency, thin layer MoS_2 are promising electronic devices[16]. Impurities, such as vacancies, chemical doping, and grain boundaries, can lead to phonon scattering[17–20] and, as a result, thermal conductivity reduction. Green's function suggests the higher likeliness of short wavelength or high-frequency phonon modes scattering by defects. Jenisha et al.[14] revealed the reduction of thermal conductivity for Ni-doped MoS_2. They observed two times smaller thermal conductivity of about 0.48 W/m·K for 7.5% of Ni-doped MoS_2 than undoped MoS_2. Mao et al.[15] reported a significant increase in electric conductivity and reduction in thermal conductivity for 1–10% vanadium atoms doped in MoS_2 lattice structure. Also, the thermal conductivity was significantly reduced due to point defects and interface scattering. Structural, optical, electrical, and phonon properties of V-doped and Ti-doped 2D MoS_2 were studied by Williamson et al.[21] They revealed the concentration of 2.083% Ti is the most effective due to effective dopant isolation. The research indicated that Ti dopant impacts the phonon properties greater than V-doped; however, V-dopant has a great phonon anharmonicity due to shorter bond length and weaker covalent bonds.

Modifying the magnetic properties of MoS_2 nanosheets is crucial for expanding their applications in nanoelectronics[22] and spintronics[23] using the diluted magnetic semiconductor (DMS) concept. MoS_2 nanosheets, however, are intrinsically nonmagnetic. Therefore, it is highly desirable to realize stable magnetism in MoS_2. Iron-doped Molybdenum disulfide (Fe:MoS_2) is considered a quantum material thanks to its intriguing properties,

[1]Department of Mechanical Engineering, Stevens Institute of Technology, Hoboken, NJ 07030, USA. [2]Center for Functional Nanomaterials, Brookhaven National Laboratory, Upton, NY 11973, USA. ✉email: xzhang4@stevens.edu

such as magnetic properties, lower mobility, more lattice impurities, and imperfections. Iron (Fe) doping into MoS_2 lattice structure has been reported to facilitate DMS formation[24], with Scanning Transmission Electron Microscopy (STEM), X-ray Photoelectron Spectroscopy (XPS), and Magnetic circular Dchroism (MCD) Spectroscopy characterizations of the Fe doping. The magnetic and electronic properties of Fe-doping monolayer MoS_2 have been studied using a combination of density functional theory by Shu et al.[25] They reported that the stability of Fe dopant in MoS_2 lattice structure depends on the layer number and chemical potential. In another work, Mishra et al.[26] investigated the electronic and magnetic properties of the Fe atom doped on the MoS_2 and MoS_2 using first-principal function theory. They reported that the dopant significantly changes magnetic moments, magnetic anisotropic energy, and charge transfer which counts as electronic properties. Wang et al.[11] compared undoped and Fe-doped MoS_2 chemical vapor deposition (CVD) grown optical and electrical properties. They observed longer carrier lifetime and lower mobility for Fe:MoS_2 compared to MoS_2. Despite all the studies on Fe:MoS_2, the thermal transport properties of Fe:MoS_2 has not been extensively investigated. The findings could be used to design Fe doped MoS_2 electronic devices in the future.

In this work, we report the in-plane thermal conductivity of 1L, 2L, and 3L Fe:MoS_2 and the interfacial thermal conductance between the Fe:MoS_2 and SiO_2 substrate for the first time. The opto-thermal Raman technique is employed to measure the thermal properties[27,28] of Fe:MoS_2. This technique is contactless, with no fabrication requirement and capable of directly measuring thermal conductivity without changing the physical properties of pristine samples. It is particularly ideal for measuring 2D materials due to their sub-nanometer thickness. The result has been confirmed by the computational method, density theory function.

Results

MoS_2 monolayers were synthesized via Low pressure chemical vapor deposition (LPCVD). The schematic of growth using the chemical vapor deposition is shown in Fig. 1, and the details are described in the Methods section.

The morphology of the Fe:MoS_2 samples was characterized by optical microscopy and scanning electron microscopy as shown in Figs. 2a and b, respectively. To confirm the growth of 1-3L Fe:MoS_2 domains, the sample is characterized by the atomic force microscopy (AFM) peak force mode (Bruker Dimension) as shown in Fig. 2c. The thicknesses of 1L, 2L, and 3L Fe:MoS_2 are 0.8 nm, 1.6 nm, and 2.4 nm. The AFM image also confirms that there is no Fe_3O_4 residual remaining on the surface of Fe:MoS_2 after wet cleaning and thermal annealing. Figure 2d is the top view schematic of crystal structure of Fe:MoS_2.

Raman and photoluminescence (PL) spectroscopy provide evidence that Fe is incorporated into the lattice (Fig. 2). To demonstrate the success of doping MoS_2 with Fe, the photoluminescence (PL) spectra of the 1L MoS_2 and Fe:MoS_2 were characterized under a 405 nm laser excitation with 5 mW power at 300 K. There are two broad bands in the PL spectrum associated with two excitons peaks formed by spin–orbit coupling in the valence band (direct excitonic transition). The left PL peak at 1.86 eV represents MoS_2 and the right peak at 1.49 eV represents Fe in Fe:MoS_2. The red-shift of 0.37 eV caused by defect in MoS_2 lattice structure. Figure 2e shows that the PL intensity of the Fe:MoS_2 sample dropped significantly compared to the MoS_2 sample. This optical quenching results from the MoS_2 lattice distortion due to the introducing of the Fe dopants into the lattice and the existence of additional nonradiative channels known as trap states[11,29].

Due to the highly mobile charges and wide access to shallow trap states, MoS_2 is expected to have more electron concentration when Fe dopants are introduced. Fe is an n-type dopant, so Fe-doping is expected to increase electron concentrations in Fe:MoS_2 monolayers. Due to the reduction in neutral excitons and the increase in negative trion emission, the peak position of the PL would be redshifted, as previous studies demonstrated[30]. The spectra of 1L MoS_2 and 1L Fe:MoS_2 samples were collected using a micro-Raman spectrometer (Renishaw InVia Raman Microscope system) under 514 nm laser excitation. Both spectra demonstrate the in-plane E^1_{2g} and out-of-plane A_{1g} vibration modes of MoS_2 as shown in Fig. 2f. The E^1_{2g} and A_{1g} models of the pristine MoS_2 sample are at 385.4 cm^{-1} and 404.6 cm^{-1}, respectively. The A_{1g} model of the Fe:MoS_2 is at 404.2 cm^{-1}, which is like that of the pristine MoS_2. However, the E^1_{2g} model of the Fe:MoS_2 is at 381.1 cm^{-1}, indicating a red shift as

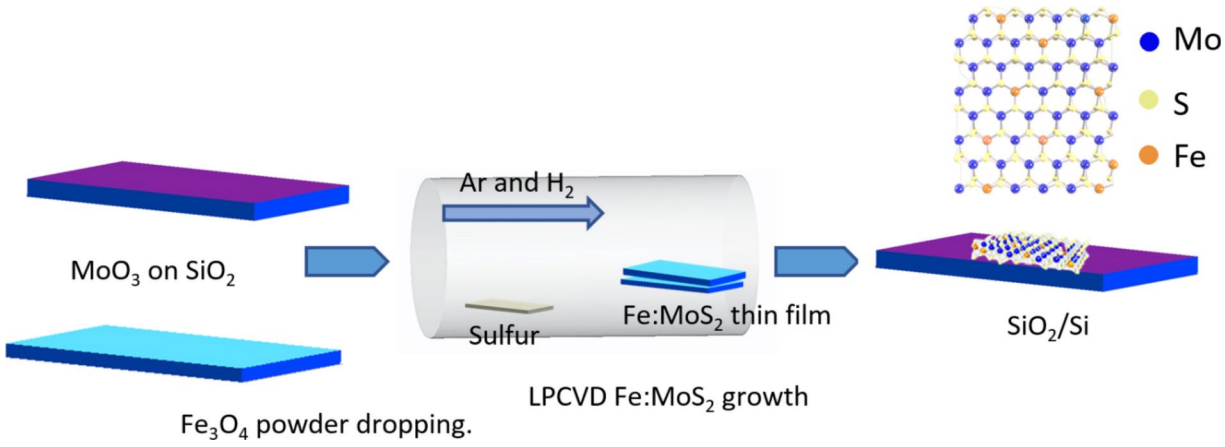

Fig. 1. Schematic of chemical vapor deposition (CVD) growth process for Fe:MoS_2.

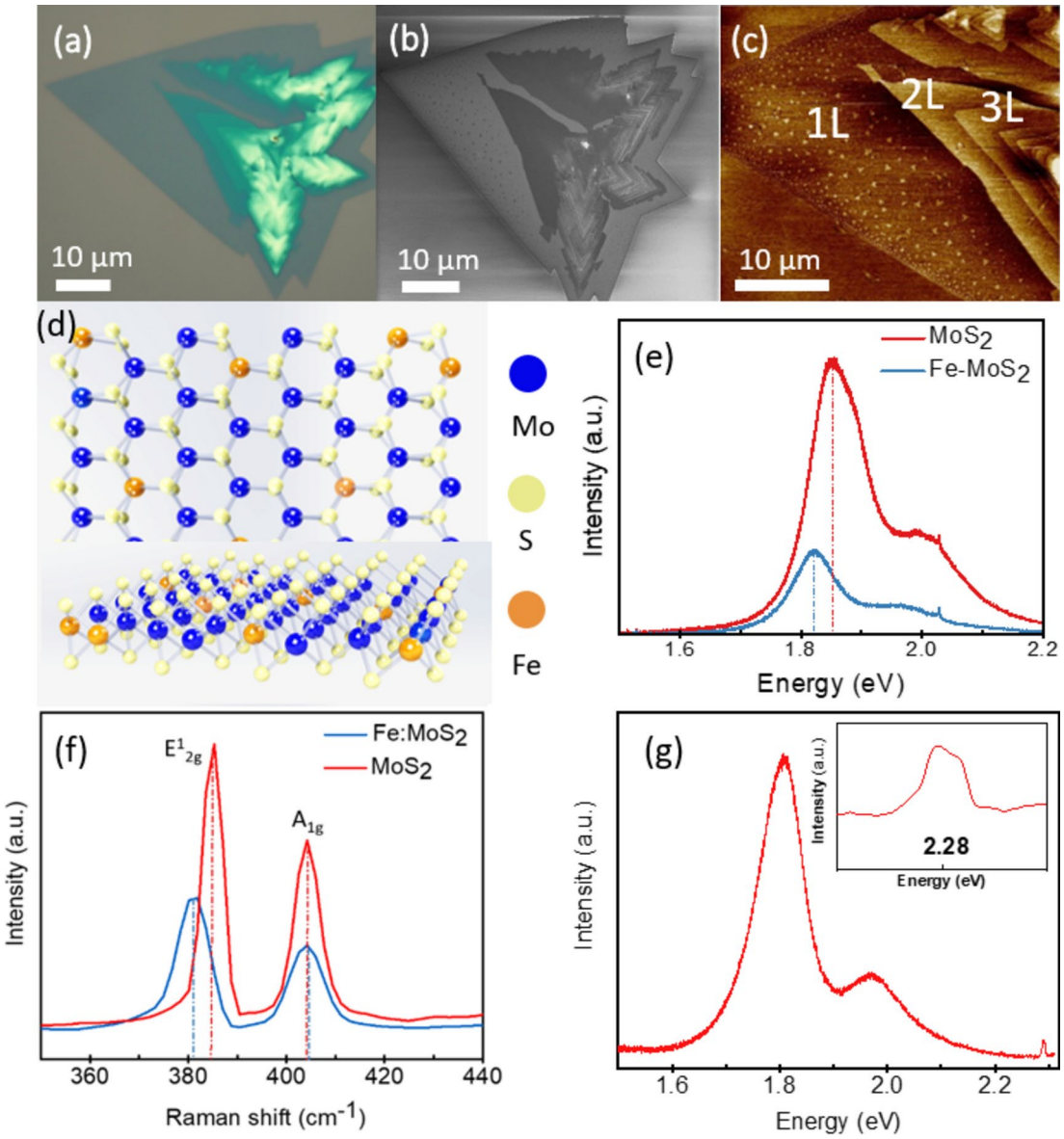

Fig. 2. (**a**) Optical microscopy image of 1–3L Fe:MoS_2. (**b**) Scanning electron microscopy image of 1-3L Fe:MoS_2. (**c**) Atomic force microscopy image of 1–3L Fe:MoS_2. (**d**) Top view schematic of crystal structure of Fe:MoS_2. (**e**) Photoluminescent spectra and (**f**) Raman spectra comparing MoS_2 and Fe:MoS_2 monolayers. (**g**) PL spectra of 1L Fe:MoS_2 at 300 K. Only Fe:MoS_2 monolayers exhibit Fe-related emission (2.28 eV), whereas undoped MoS_2 with Fe and Fe_3O_4 clusters on top does not. This finding suggests that only substitutional incorporation of Fe can produce this transition.

compared with that of the MoS_2. The observed red-shift can be related to the defect in MoS_2 lattice structure[16]. In addition, Raman spectroscopy was employed to further confirm that Fe incorporates into the MoS_2 lattice. Figure 2g presents a comparison of PL emission for MoS_2 and Fe:MoS_2. It is clear from this figure that the Fe-related emission at 2.28 eV can only be observed from 1L Fe:MoS_2[16], which also validates the substitution of Mo by Fe atoms and there is no peak at 2.28 eV for 1L MoS_2. This peak is only observable for 1L Fe:MoS_2 at room temperature since 2.28 eV peak is considered as PL emission and is affected by band gap. The band gap changes from direct to indirect as the layer number increases from monolayer to thicker samples. Therefore, the quench for the 2.28 eV peak disappears for samples thicker than 1L[31].

Figure 3a presents a schematic of the experimental setup for the Fe:MoS_2 sample by the opto-thermal Raman technique, while in Fig. 3b a schematic of the Raman laser and thermal transport profiles can be observed. At temperatures ranging from 303 to 423 K, we calibrated the Raman E^1_{2g} peak position shift rate. A laser with a wavelength λ of 514 nm was used. A Raman spectrum of 1L Fe:MoS_2 with temperature dependence is shown in Fig. 3c.

To acquire χ_P (power-dependent coefficient), the E^1_{2g} mode shift of the Fe:MoS_2 samples was also measured using the micro-Raman system under the 514 nm laser excitation. Then the power dependent coefficient can

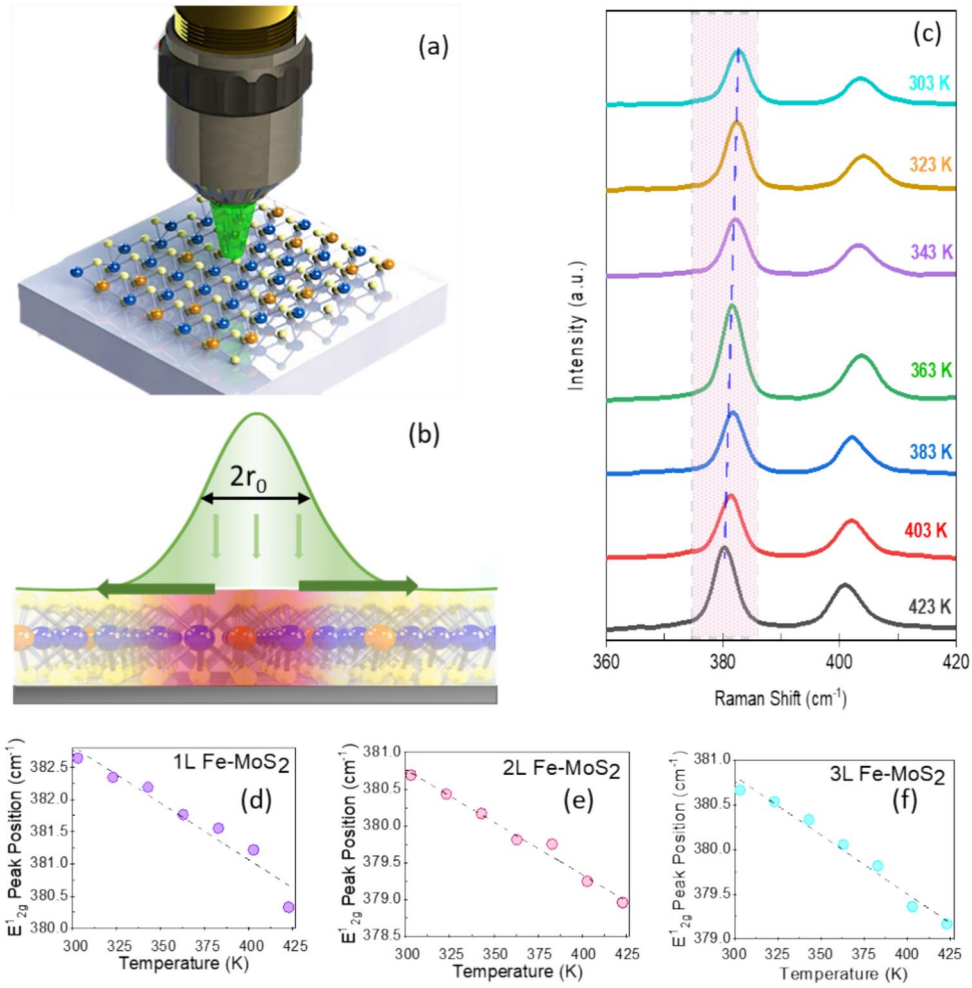

Fig. 3. (**a**) Schematic of the experimental setup for the Fe:MoS_2 sample by the opto-thermal Raman technique. (**b**) Schematic of the Raman laser and thermal transport profiles. (**c**) Raman spectra of 1L Fe:MoS_2 recorded at temperatures from 303 to 423 K. (**d**) The temperature-dependent E^1_{2g} Raman peak shift measured on the 1L Fe:MoS_2, (**e**) 2L Fe:MoS_2, and (**f**) 3L Fe:MoS_2.

be derived from the equation of $\omega(P) = \omega_0 + \chi_P P$, where $\omega(P)$ is the Raman peak frequency at absorbed laser power P, ω_0 is the Raman peak frequency at power 0 and P is the absorbed laser power. The absorbed laser power can be calculated by multiplying the incident laser power with the absorbance (α) of the samples. The confocal absorption spectra were recorded with a Nikon Eclipse TE2 equipped with an Acton 500 spectrograph and a PIXIS 100 CCD camera (NT&C Consulting, Germany). Figure 4a shows the absorbance of the 1L, 2L, and 3L Fe:MoS_2 as a function of wavelength. We used the interpolated method to extract the absorbance at 514 nm wavelength. The absorbance values of 1L, 2L, and 3L Fe:MoS_2 are 0.0127, 0.0344, and 0.0831, respectively. 1L-3L Fe:MoS_2 were prepared on a transparent quartz substrate, and the transmittance T of 1L-3L Fe:MoS_2 at the wavelength of 480 nm – 800 nm were characterized. The absorbance A were calculated as $A = log10(1/T)$. The E^1_{2g} peak position as a function of the absorbed laser power was characterized using both 100× and 50× objective lens of the Raman system as shown in Fig. 4b, c, and d. The laser light acted as both the thermometer and the heat source for the Fe:MoS_2 flakes. It can be observed that the E^1_{2g} peak of all the samples decreases almost linearly as a function of the absorbed laser power. This is because the local temperature rise induced by the laser heating resulted in red shift due to the phonon softening effect. The convection through the air is negligible since it is less than 0.01% for all the measured samples[18]. Both χ_T and χ_P are extracted via linear regression and summarized in Table 1.

To calculate the thermal conductivity, one also need to know the laser spot size of the Raman system. The laser spot size of both 100× and 50× objective lenses was measured using the knife-edge method[32]. In this method, the laser moves across a sharp edge and using the Raman mapping feature the Si peak is monitored. The Si peak intensity as a function of position had been studied with Gaussian distribution as mentioned in equation below

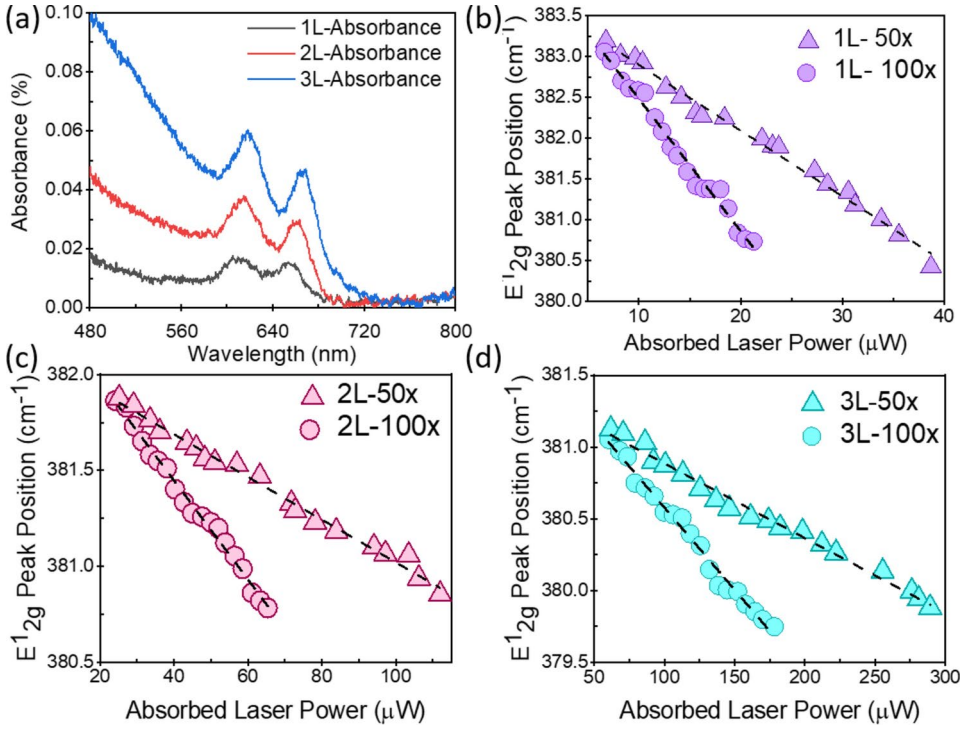

Fig. 4. (**a**) Absorbance of 1-3L Fe:MoS_2 at wavelengths from 480 to 800 nm. (**b**) Power-dependent $E_{2g}{}^1$ Raman peak shift characterized using two different laser spot sizes, on the 1L Fe:MoS_2, (**c**) 2L Fe:MoS_2, and (**d**) 3L Fe:MoS_2.

	Temperature coefficient (cm^{-1}/K)	Absorbance (%)	Absorbed power shift rate (cm^{-1}/μw)	
			0.18 μm spot size	0.31 μm spot size
1L Fe:MoS_2	−0.0176 ± 0.0020	1.27	−0.1185 ± 0.0036	−0.0644 ± 0.00150
2L Fe:MoS_2	−0.0143 ± 0.0008	3.44	−0.0383 ± 0.0009	−0.0182 ± 0.00004
3L Fe:MoS_2	−0.0131 ± 0.0008	8.31	−0.0158 ± 0.0004	−0.0067 ± 0.00004

Table 1. First-order temperature coefficients, absorbance, and power shift rates of 1–3L Fe:MoS_2.

$$I = I_0 expexp\left(\frac{(x - x_c)^2}{r_0^2}\right) \tag{1}$$

where r_0 is the laser spot size, x_c is the center of peak position, and I_0 is the initial intensity. The laser spot size passing through 100× and 50× was 0.18 μm and 0.31 μm, respectively. The measurements were made in the air at ambient temperature. Laser spot size can also be estimated from the numerical aperture. $r_0 = \frac{\lambda}{\pi . NA}$ where λ is the laser wavelength and NA is the numerical aperture. For 100× and 50×, the calculated result using the numerical aperture is 0.19 μm and 0.22 μm, respectively. The substrate interaction can make the mean free paths of phonons in Fe:MoS_2 smaller than the laser beam size, especially for long-wavelength phonons[33]. In the cylindrical coordinate T(r), the temperature distribution is related to the in-plane thermal conductivity, interfacial thermal conductance between the flake and substrate, and the absorbed laser power. The volumetric laser heating power density $q'''(r)$ based on the Gaussian profile of the laser equation below is

$$q'''(r) = \frac{p}{t.\pi r_0^2} expexp\left(\frac{-r^2}{r_0^2}\right) \tag{2}$$

where P is the absorbed laser power, t is the thickness of the flake, and r_0 is the laser spot size. After taking the interfacial thermal conductance between the flake and the substrate into consideration, T(r) is presented by the equation below

$$\frac{1}{r}\frac{d}{dr}\left(r\frac{dT(r)}{dr}\right) - \frac{g}{k_s t}(T(r) - T_a) + \frac{q'''(r)}{k_s} = 0 \tag{3}$$

	Thermal conductivity (W/m·K)		
	At 300 K	At 500 K	Interfacial thermal conductance (MW/m²·K)
1L Fe:MoS_2	24 ± 11	19 ± 10	0.3 ± 0.2
2L Fe:MoS_2	18 ± 9	11 ± 6	1.1 ± 0.7
3L Fe:MoS_2	16 ± 8	8 ± 3	3.0 ± 2.3

Table 2. Thermal conductivities of 1–3L Fe:MoS_2 at room temperature (300 K) and at 500 K, and their interfacial thermal conductance.

where g is the interfacial thermal conductance between the flake and the substrate, K_s is the in-plane thermal conductivity of Fe:MoS_2 and T_a is the ambient temperature. The weighted result can be calculated by considering the Gaussian profile of the laser spot. The equation below is the average temperature.

$$T_m = \frac{\int_0^\infty T(r)\, exp\left(\frac{-r^2}{r_0^2}\right) rdr}{\int_0^\infty exp\left(\frac{-r^2}{r_0^2}\right) rdr} \tag{4}$$

To solve the equations, boundary conditions need to be defined. Based on the Gaussian profile of the laser $\frac{dT}{dr}|_{r=0} = 0$, the maximum temperature is in the center where the laser shines on the sample ($T(r=0) = T_{max}$ and further away from the center, the temperature is the ambient temperature $T(r \to \infty) = T_a$. We also need to calculate the thermal resistance of Fe:MoS_2, which can be calculated as $R_m = \frac{T_m}{P}$ and relate the thermal resistance to the thermal conductivity and the interfacial thermal conductance between the flake and the substrate. The ratio of two R_m characterized from two laser spot sizes is a function of g/K_s. The calculated results are $K_s = 24 \pm 11$ W/m·K, and $g = 0.3 \pm 0.2$ MW/m²·K for 1L Fe:MoS_2, $K_s = 18 \pm 9$ W/m·K, and $g = 1.1 \pm 0.7$ MW/m²·K for 2L Fe:MoS_2, and $K_s = 16 \pm 8$ W/m·K, and $g = 3.0 \pm 2.3$ MW/m²·K for 3L Fe:MoS_2.

To obtain the relationship between Raman peak shift and temperature rise, we also heated the samples from room temperature to 500 K on the heating platform. The optothermal Raman characterizations were conducted with a Raman laser of low power (100 μW). The thermal conductivity and interfacial thermal conductance between the flake and substrate are summarized in Table 2.

Discussion

Thermal conductivities of 1-3L Fe:MoS_2 have been explored and found in the range of 16–24 W/m·K which is about 40% lower than the reported values for MoS_2[18]. This value is also smaller than other TMDC materials, such as MoS_2, $MoSe_2$, and WSe_2, due to the imperfect lattice structure of MoS_2 from the doping engineering. The iron doped MoS_2 causes imperfection in the lattice structure, leading to phonon scattering and a further reduction in thermal conductivity. The phonon scattering rate caused by imperfections can be derived from Green's function approach or calculated using Fermi's golden rule[34,35]. The phonon scattering rate for 2D materials can be estimated by the formula $\frac{1}{\tau_{qs}^D} \propto \left(\frac{\omega^3}{v^2}\right) \sum_i f_i \left[(1 - \frac{m_i}{m})^2 + \varepsilon(\gamma(1 - \frac{r_{a,i}}{r_a})^2\right]$, where m and r_a are the average atom mass and radius, υ is the phonon group velocity, γ is the Gruneisen parameter, mi, ra, i, and fi are the mass, radius, and fraction concentration of type i atom, and ε is a parameter for defect scattering due to lattice distortion and mass difference. This expression indicates the likelihood of high-frequency phonon modes scattering by defects. Since the Fe atoms substitute the Mo atoms in MoS_2 lattice structure, the difference between the atomic radius and the atomic mass of these two materials cause a change in phonon scattering rate[36].

A decreasing trend of thermal conductivities and an increasing trend in interfacial thermal conductance have been observed with increasing layer numbers of Fe:MoS_2. The decreasing trend of thermal conductivities from thinner layer to thicker layer is due to the stronger phonon-boundary scattering. The strength of boundary condition scattering, which is defined as $\Gamma_{qs}^B \propto \frac{|v_{qs}|}{t}$ where t is the thickness, decreases in the layered 2D crystals due to the weak van der Waals interaction [36]. In addition, the decreasing trend is associated with the Umkkalpp phonon scattering, crystal's phonon anharmonicity, and reduction of ballistic resistance that affects phonon mean free path for thicker flakes. Other studies on the MoS_2, $MoSe_2$, WSe_2, and hBN also faced the decreasing trend of thermal conductivity with increasing the number of layers[18,37,38]. The increasing trend in interfacial thermal conductance could be explained that as the number of layers increases, the interface between 2D materials and the substrate becomes more tightly coupled. In addition, there are less defects in 2D materials with increased layers because more layers can act as "bridge" between 2D materials and the substrate. We also compared to the undoped CVD MoS_2 that we synthesized with the Fe doped CVD MoS_2 in this work(with Fe concentration 0.3–0.5%), and found the Fe doped CVD MoS_2's thermal conductivity is ~30% smaller. This decrease in thermal conductivity is due to the defects in the material created during the doping process.

Computational studies were carried out in parallel to verify the experimental results. we utilized a combination of phonopy, thirdorder, and ShengBTE software, integrated with VASP first-principles DFT calculations, to compute the thermal conductivity of Fe-doped MoS_2. The second- and third-order interatomic force constants were extracted and employed to solve the phonon Boltzmann transport equation. For this, we constructed a 4×4×1 supercell of monolayer MoS_2, with one Mo atom substituted by an Fe atom to introduce

doping. Following structural optimization, the atomic configuration corresponding to the minimum energy was identified. The cutoff energy for plane-wave basis sets was set to 400 eV, ensuring sufficient accuracy, while the energy convergence criterion was set to 1×10^{-6} eV, which provided precise structural optimization. Additionally, we used a Γ-centered k-point mesh of $6 \times 6 \times 1$ for Brillouin zone sampling and employed a Methfessel-Paxton smearing method with a width of 0.05 eV to ensure electronic structure convergence during the relaxation process. the cutoff distance was set to 0.3 Å in the calculation of third-order force constants for neighboring atoms. We employed a $10 \times 10 \times 10$ q-grid to more accurately estimate phonon frequencies and phonon lifetimes, ensuring better resolution of the phonon characteristics for our calculations.

The thermal conductivity results revealed that for the monolayer Fe-doped MoS_2, the in-plane thermal conductivity was 28.3 W/mK. In contrast, for the bilayer Fe-doped MoS_2, the in-plane thermal conductivity dropped to 20.3 W/mK. The in-plane thermal conductivity of the 3L material is 18.8 W/mK. The computational results are in good agreement with the experimental findings. These findings indicate that the significant reduction in thermal conductivity for multilayered 2D materials, as compared to their monolayer counterparts, can be attributed to the poor efficiency of interlayer thermal transport. The out-of-plane thermal conductivity remains several orders of magnitude lower than the in-plane thermal conductivity, which is primarily responsible for the observed suppression of thermal transport in the multilayer structure.

Methods

MoS_2 monolayers were synthesized via Low pressure chemical vapor deposition (LPCVD). Before growth, a thin MoO_3 layer was prepared using physical vapor deposition (PVD) of e-beam evaporating MoO_3 pellet onto a Si substrate with 300 nm-thick thermal oxides. Subsequently, the MoO_3-deposited substrate was in direct contact with a different SiO_2/Si substrate. On the SiO_2/Si substrate, monolayers of Fe:MoS_2 were grown. The following steps were taken to dope the Fe atoms: the MoO_3-deposited substrate was rinsed with deionized (DI) water to deposit a thin layer of water on the SiO_2 surface to ensure that the Fe_3O_4 particles were distributed uniformly. Fe_3O_4 particles were uniformly cast onto the SiO_2/Si substrate and then the substrate was baked at 110 °C for 5 min. During the growth, the furnace was heated with a ramping rate of 18 ˚C/min and held for 15 min at 850 ˚C. Upon the heating procedure, an argon gas (30 sccm) was supplied at 300 ˚C, and a hydrogen gas (15 sccm) was delivered at 760 ˚C. Sulfur was supplied when the furnace temperature reached 790 ˚C. After the growth, a few millimeters of Fe:MoS_2 monolayers were obtained.

Conclusion

It is the first work to explore the thermal transport properties of the novel magnetic 2D material Fe:MoS_2 in its 1L to 3L forms, both experimentally and computationally. Fe:MoS_2 is produced via the LPCVD method, with Fe atoms in the lattice structure of Fe:MoS_2 characterized by Raman spectroscopy and photoluminescence. Our refined opto-thermal Raman method was used to characterize the in-plane thermal conductivity and interfacial thermal conductance of Fe:MoS_2. A decreasing trend has been observed for thermal conductivities of Fe:MoS_2 as the layer number increases. The in-plane thermal conductivities of 1L, 2L, and 3L Fe:MoS_2 are 24 ± 11 W/m·K, 18 ± 9 W/m·K, and 16 ± 8 W/m·K and the interfacial thermal conductivity are 0.3 ± 0.2 MW/m^2·K, 1.1 ± 0.7 MW/m^2·K, and 3.0 ± 2.3 MW/m^2·K respectively. These values will help us to understand their thermal behavior, the critical factor that has a significant limitation on nano- and quantum devices. Experimental results show a layer-dependent trend of thermal conductivity.

Data availability

The datasets used and analysed during the current study available from the corresponding author on reasonable request.

Received: 30 August 2024; Accepted: 24 December 2024
Published online: 02 January 2025

References

1. Novoselov, K. S. et al. Electric field effect in atomically thin carbon films. *Science* **306**(5696), 666–669 (2004).
2. Amani, M. et al. Recombination kinetics and effects of superacid treatment in sulfur- and selenium-based transition metal dichalcogenides. *Nano Lett.* **16**(4), 2786–2791 (2016).
3. Ahmed, S. & Yi, J. Two-dimensional transition metal dichalcogenides and their charge carrier mobilities in field-effect transistors. *Nano-Micro Lett.* **9**(4), 50 (2017).
4. Kandemir, A., Yapicioglu, H., Kinaci, A., Çağın, T. & Sevik, C. Thermal transport properties of MoS2 and MoSe2 monolayers. *Nanotechnology* **27**(5), 055703 (2016).
5. Wang, Y. & Zhang, X. Thermal transport in graphene under large mechanical strains. *J. Appl. Phys.* **136**(7), 074302 (2024).
6. Ye, F., Liu, Q., Xu, B., Feng, P. X. L. & Zhang, X. Ultra-high interfacial thermal conductance via double hBN encapsulation for efficient thermal management of 2D electronics. *Small* **19**(12), 2205726 (2023).
7. Kalantari, M. H., Zhang, X. Thermal transport in 2D materials. *Nanomaterials* [Online] (2023).
8. Wang, Y. & Zhang, X. On the role of crystal defects on the lattice thermal conductivity of monolayer WSe2 (P63/mmc) thermoelectric materials by DFT calculation. *Superlattices Microstruct.* **160**, 107057 (2021).
9. Seyler, K. L. et al. Electrical control of second-harmonic generation in a WSe2 monolayer transistor. *Nature Nanotechnol.* **10**(5), 407–411 (2015).
10. Babaei, H., Khodadadi, J. M. & Sinha, S. Large theoretical thermoelectric power factor of suspended single-layer MoS2. *Appl. Phys. Lett.* **105**(19), 193901 (2014).
11. Wang, S. Y., Ko, T. S., Huang, C. C., Lin, D. Y. & Huang, Y. S. Optical and electrical properties of MoS2 and Fe-doped MoS2. *Japanese J. Appl. Phys.* **53**(4S), 04EH07 (2014).
12. Wang, Y., Zhang, X. Experimental and theoretical investigations of direct and indirect band gaps of WSe2 *Micromachines* [Online] (2024).

13. Mas-Ballesté, R., Gómez-Navarro, C., Gómez-Herrero, J. & Zamora, F. 2D materials: To graphene and beyond. *Nanoscale* **3**(1), 20–30 (2011).
14. Jenisha, M. A. et al. Interfacial engineering effect and bipolar conduction of Ni- doped MoS2 nanostructures for thermoelectric application. *J. Alloys Compd.* **895**, 162493 (2022).
15. Mao, Y., Fang, Y., Yuan, K. & Huang, F. Effect of vanadium doping on the thermoelectric properties of MoS2. *J. Alloys Compd.* **903**, 163921 (2022).
16. Chen, Y. et al. Tuning electronic structure of single layer MoS2 through defect and interface engineering. *ACS Nano* **12**(3), 2569–2579 (2018).
17. Zhou, W.-X. et al. Thermal conductivity of amorphous materials. *Adv. Funct. Mater.* **30**(8), 1903829 (2020).
18. Chen, X.-K., Zhang, E.-M., Wu, D. & Chen, K.-Q. Strain-induced medium-temperature thermoelectric performance of Cu_4TiSe_4: The role of four-phonon scattering. *Phys. Rev. Appl.* **19**(4), 044052 (2023).
19. Chen, X.-K. et al. Large contributions from optical phonons to thermal transport in hexagonal carbon-boron-nitrogen monolayers. *Phys Rev B* **108**(23), 235420 (2023).
20. Kuang, H.-L., Wu, C.-W., Zeng, Y.-J., Chen, X.-K. & Zhou, W.-X. The amplification effect of four-phonon scattering in CdX (X=Se, Te): The role of mid-frequency phonons. *Int. J. Thermal Sci.* **205**, 109254 (2024).
21. Williamson, I. et al. Structural, electrical, phonon, and optical properties of Ti- and V-doped two-dimensional MoS2. *Chem. Phys. Lett.* **674**, 157–163 (2017).
22. Yokoo, A. Nanoelectrode lithography. *Jpn. J. Appl. Phys.* **42**(2A), L92 (2003).
23. Zibouche, N., Kuc, A., Musfeldt, J. & Heine, T. Transition-metal dichalcogenides for spintronic applications. *Ann. der Phys.* **526**(9–10), 395–401 (2014).
24. Fu, S. et al. Enabling room temperature ferromagnetism in monolayer MoS2 via in situ iron-doping. *Nature Commun.* **11**(1), 2034 (2020).
25. Shu, H., Luo, P., Liang, P., Cao, D. & Chen, X. Layer-dependent dopant stability and magnetic exchange coupling of iron-doped MoS2 nanosheets. *ACS Appl. Mater. Interfaces* **7**(14), 7534–7541 (2015).
26. Mishra, N., Pandey, B. P. & Kumar, S. Impact of Mn- and Fe-doping on electronic and magnetic properties of MoX_2 (X = S, Se) monolayer. *IEEE Trans. Electron Devices* **69**(3), 1553–1560 (2022).
27. Zhang, X. et al. Measurement of lateral and interfacial thermal conductivity of single- and bilayer MoS2 and MoSe2 using refined optothermal Raman technique. *ACS Appl. Mater. Interfaces* **7**(46), 25923–25929 (2015).
28. Easy, E. et al. Experimental and computational investigation of layer-dependent thermal conductivities and interfacial thermal conductance of one- to three-layer WSe2. *ACS Appl. Mater. Interfaces* **13**(11), 13063–13071 (2021).
29. Zhang, S. et al. Controllable, wide-ranging n-doping and p-doping of monolayer group 6 transition-metal disulfides and diselenides. *Adv. Mater.* **30**(50), 1806345 (2018).
30. Mouri, S., Miyauchi, Y. & Matsuda, K. Tunable photoluminescence of monolayer MoS2 via chemical doping. *Nano Lett.* **13**(12), 5944–5948 (2013).
31. Zhang, K. et al. Tuning the electronic and photonic properties of monolayer MoS2 via in situ rhenium substitutional doping. *Adv. Funct. Mater.* **28**(16), 1706950 (2018).
32. Suzaki, Y. & Tachibana, A. Measurement of the μm sized radius of Gaussian laser beam using the scanning knife-edge. *Appl. Opt.* **14**(12), 2809–2810 (1975).
33. Xiaokun Gu, R. Y. Phonon transport and thermal conductivity in two-dimensional materials. In: Annual Review of Heat Transfer, Begell: 2016.
34. Klemens, P. G., The scattering of low-frequency lattice waves by static imperfections. *Proceedings of the Physical Society. Section A* **1955,** *68* (12), 1113.
35. Klemens, P. G. Theory of the a-plane thermal conductivity of graphite. *J. Wide Bandgap Mater.* **7**, 332–339 (2000).
36. Yarali, M. et al. Effects of defects on the temperature-dependent thermal conductivity of suspended monolayer molybdenum disulfide grown by chemical vapor deposition. *Adv. Funct. Mater.* **27**(46), 1704357 (2017).
37. Cai, Q., Scullion, D., Gan, W., Falin, A., Zhang, S., Watanabe, K., Taniguchi, T., Chen, Y., Santos, E. J. G., Li, L. H. High thermal conductivity of high-quality monolayer boron nitride and its thermal expansion. *Sci. Adv.* *5*(6), eaav0129.
38. Yuan, P., Wang, R., Wang, T., Wang, X., Xie, Y. Nonmonotonic thickness-dependence of in-plane thermal conductivity of few-layered MoS2: 2.4 to 37.8 nm. *Phys. Chem. Chem. Phys.* 2018, **20**(40), 25752–25761.

Acknowledgements

This work was supported by the National Science Foundation CAREER Award (Grant CBET-2145417) and LEAPS Award (Grant DMR-2137883).

Author contributions

X.Z. contributed to the conceptualization and the methodology. E.E. and X.Z. contributed to the investigation. M.F. and E.Y. contributed to the material synthesis. M.L. contributed to the optical characterization. E.Y. contributed to writing the original draft. X.Z. contributed to writing the review and editing. All authors have given approval to the final version of the manuscript.

Funding

National Science Foundation CAREER Award (Grant CBET-2145417) and LEAPS Award (Grant DMR-2137883).

Declarations

Competing interests

The authors declare no conflict of interest.

Additional information

Correspondence and requests for materials should be addressed to X.Z.

Reprints and permissions information is available at www.nature.com/reprints.

Publisher's note Springer Nature remains neutral with regard to jurisdictional claims in published maps and institutional affiliations.